Combining Soft with Hard Condensed Matter for Circular Polarized Light Sensing and Logic Operations

Paul Grey, Manuel Chapa, Miguel Alexandre, Tiago Mateus, Elvira Fortunato, Rodrigo Martins, Manuel J. Mendes, and Luís Pereira*

The study shows the incorporation of chiral nematic photonic cellulose nanocrystal (CNC) films, well known for their adaptive character of selective reflection of circular polarized light (CPL), and silicon-based thin-film photodiodes, thus achieving a light sensor capable of discriminating right- from left-handed CPL. The circular polarization (CP) response is maximum for specific wavelengths in the green-to-red region. When subjected to these wavelengths, they produce photocurrents that are over 50% distinct between the two CP states. Proper signal processing, thus, yields a binary output depending on the handedness of the light. Through the addition of monovalent salt to the initial CNC suspension, a blueshift to the photonic band gap is induced, enabling a larger wavelength gamut and application possibilities. The measured results are then used as a basis for electromagnetic simulations that show remarkable consistency with the experimental results, thus defining a new tool that can be used to efficiently optimize the devices' response. Fast transient responses to CPL are shown with possible logic operations, as well as humidity sensing. The developed devices are, thus, applicable in areas as diverse as imaging, CPL sensing, optoelectronic counterfeiting, and information processing with logic states that depend solely on the handedness of the incident light.

1. Introduction

Circular polarized light (CPL) has seen an increased interest in the area of chiroptical sensing due to its strong interaction with systems that lack mirror symmetry.[1] The chirality of left- and right-handed CPL (LCPL and RCPL, respectively) potentiates its interaction with systems that are structurally similar.

P. Grey, M. Chapa, M. Alexandre, T. Mateus, Prof. E. Fortunato,
Prof. R. Martins, Prof. M. J. Mendes, Prof. L. Pereira
i3N/CENIMAT
NOVA School of Science and Technology (FCT-NOVA)
Universidade NOVA de Lisboa
Campus de Caparica, Caparica 2829-516, Portugal
E-mail: lmnp@fct.unl.pt
Prof. L. Pereira
AlmaScience
Campus da Caparica, Caparica 2829-516, Portugal

ⓘ The ORCID identification number(s) for the author(s) of this article can be found under https://doi.org/10.1002/adom.202001731.

Chiral systems, thus, favor light propagation or interaction with one handedness over the other, which brings great advantages in, for instance, the field of enantio-chemistry, where chiral molecules behave much differently from their mirror counterpart.[2] Different approaches are used to tackle efficient implementation of structures capable of transducing chiroptical signals, such as metamaterials, asymmetric optical cavities, or chiral structured thin films.[3–6]

It is known that the polarization of light can be used as an efficient information carrier. Examples of information exchange using polarized light (linear or circular) can be found in biology with polarizing vision in stomatopods, cephalopods, crickets, or bees,[7–10] but also in modern information technology.[11–15] More specifically for CPL, the two polarization states (left and right) find application in advanced fields, such as spintronics.[16] As such, the potential use of CPL in information technology is recognized; however, emissions and detections without bulky optical elements has been a great challenge and is not an option in a miniaturization-oriented society.

Cellulose nanocrystals (CNCs), when properly processed, self-assemble into chiral nematic films with interesting photonic properties, such as iridescence and selective reflection of CPL.[17–21] These properties are connected to an inherent right-handed twisting of the CNCs on the atomic scale,[22,23] which translates to an overall left-handedness in dry films. Consequently, LCPL is reflected and RCPL is transmitted. These properties confer interesting perspectives upon usage in optoelectronic devices, capable of transducing these photonic responses.[24,25] Hence, with cellulose being the most abundant biopolymer on earth and the ease of fabricating chiral CNC films through a simple evaporation-induced self-assembly (EISA) process, they present a viable alternative to some of the more sophisticated approaches mentioned before.

The combination of chiral CNC films with optically sensitive materials, such as semiconductors, presents a viable method to access information that can be encoded in the circular polarization of light and decoded by these films. To the best of our knowledge, no works are currently focused on such endeavors, where a clear research gap can be identified. Therefore, this work focuses on the implementation of CNC films into amorphous hydrogenated silicon (a-Si:H) thin-film

**ADVANCED
SCIENCE NEWS**

www.advancedsciencenews.com

**ADVANCED
OPTICAL
MATERIALS**

www.advopticalmat.de

photodiodes (TFPs), where distinct electronic signals can be read out, depending on the circular polarization (CP) state of the incident light. The TFPs layer structure is that of a typical a-Si:H solar cell tuned to exhibit a suitable response.[26] The CNC films are characterized on behalf of their morphology by scanning electron microscopy (SEM) and their optical properties through polarized optical microscopy (POM) and spectrophotometry. The final devices are analyzed by angular spectral response (SR) with CPL in order to identify their sensitivity to distinct CP states. To better understand the underlying photonic interactions and the obtained experimental results, simulations were conducted using the software FDTD Solutions from Lumerical.[27,28] These electromagnetic simulations are not only a method to verify the experimental results but can, most importantly, be employed to extrapolate and design the right device architectures, characteristics, and responses for different purposes. Finally, some possible applications for these types of devices are introduced, focusing on time transient CPL sensing, humidity response, and logic signal conditioning with CPL.

2. Results and Discussion

Figure 1a–e shows a complete fabrication flow diagram of the devices, starting off with a TFP on glass (fabrication procedure detailed in the Experimental Section). Figure 1e shows the aspect of the final device and a magnification of its active area through a LCPL filter, where the characteristic iridescent color of the CNC film can be clearly identified. The underlying working principle of this device is derived from the selective reflection and transmission of LCPL and RCPL as schematically depicted in Figure 1g. Whereas LCPL is mostly reflected by the photonic structure, RCPL is transmitted and reaches the active area of the TFP, giving rise to a measurable photocurrent (I_{ph}). The self-assembly process, through which the photonic films are formed, is kinetically driven, where tactoids (anisotropic spherical droplets in isotropic media, see Figure S1, Supporting Information) first nucleate, then coalesce, and finally merge to give long-range ordering.[29] The merging of the tactoids and the resulting hierarchical ordering gives monodomains with distinct pitches (full rotation of the chiral nematic vector) and orientations inside the films. These monodomains are often observed as mosaic-like structure in solid CNC films (observed in Figure 1f). Hence, the final hierarchical structure is not perfect and shows defects in the form of pitch misalignments between domains and along the film (see Figure 1h), which leads to a CPL distinction (ΔCPL) well below 100%. Throughout this work, we determine ΔCPL as following

$$\Delta CPL = \frac{|I_1 - I_2|}{I_{max}} \qquad (1)$$
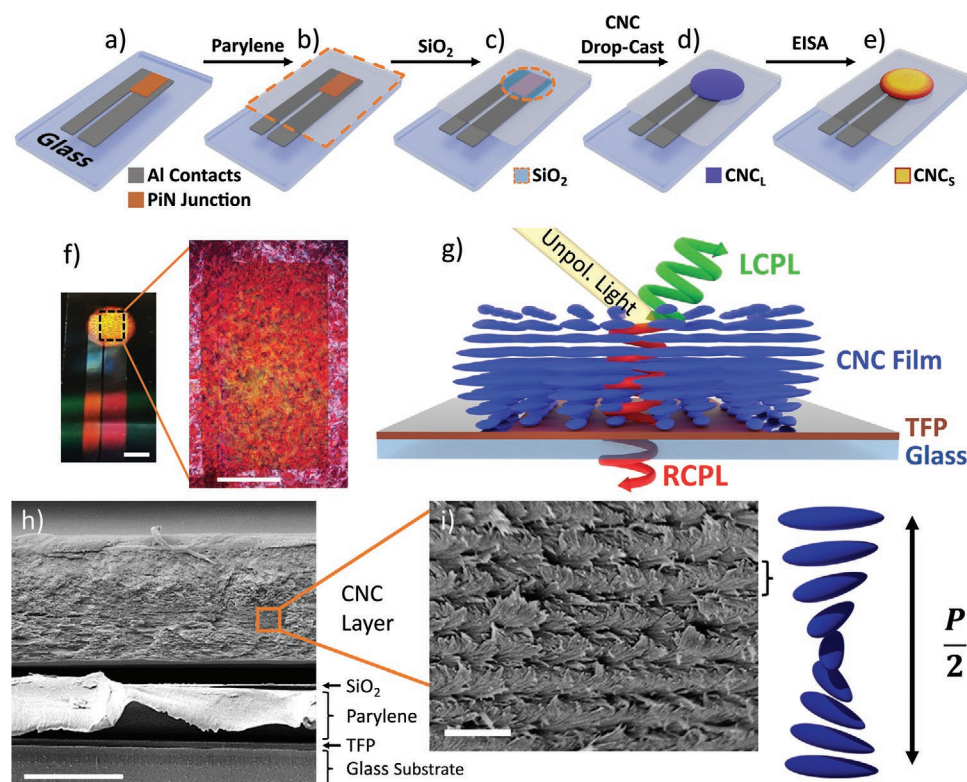

Figure 1. Device fabrication and schematization. a–e) Schematic flow diagram of the device fabrication. CNC_L and CNC_S denote liquid and solid films, respectively. f) Photograph of the final device with a CNC0 photonic film and zoom on the indicated area to show the iridescent film over the device's active area. Scale bars indicate 3 and 1.5 mm, respectively. g) Schematic representation of the underlying CPL filtering. h) Cross-sectional SEM image with identification of the device's individual layers. Scale bar represents 10 μm. i) Amplification of the indicated area in (h) with insight into the chiral nematic ordering along the photonic film. Scale bar represents 800 nm. The schematic shows a half-pitch rotation of individual CNCs along the helix.

where I_1 and I_2 are the values of the figure of merit in study (in this work, reflectance or SR) and I_{max} is the respective maximum value. Due to the defects inside the CNC films, not all LCPL is reflected, a part is in fact transmitted and reaches the TFP. Nevertheless, it was possible to constantly reach ΔCPL well above 50%, giving enough discrepancy for these devices to distinguish between the two CP states.

Figure 1h shows a SEM cross-sectional image, where each layer can be clearly identified. For EDS analysis and close-up images of the TFP, refer to Figure S2, Supporting Information. The micro-gap between the CNC and the SiO$_2$ layers was induced during sample preparation and does not reflect the aspect of the real device. Figure 1i shows the marked area in Figure 1h to show the repeated left-handed twisting along the film, giving rise to the CPL response.

Silicon presents a high absorption coefficient for wavelengths below 1000 nm, and as such is suitable for photosensing applications in such ranges.[30] Thus, by inducing minor shifts in the photonic band gap of the CNC films in said range, we can tune the responsivity of the devices for different wavelengths—and different applications. Different techniques have been shown to tune the photonic band gap (equivalent to an increase or decrease of the pitch) of films made of self-assembled CNCs.[21,31]

Our pristine CNC films present peak reflectance (λ_{peak}, at maximum ΔCPL) in the red region of the spectrum ($\lambda_{peak} \approx$ 600 nm) and therefore a simple way to blueshift the band gap is the addition of monovalent salts,[32,33] which affect the electric double layer (EDL) charges of individual CNCs and consequently their interparticle repulsion. The CNCs' surface charges are very sensitive to minor changes in ionic strength, and thus adding small quantities of NaCl (on the order of mmol kg$_{CNC}^{-1}$) decreases interparticle distances and blueshifts the photonic band gap. For this work the CNCs' response to NaCl was studied in order to tune the photonic band gap without promoting gelation (excessive salt addition).[34–37]

Initial blueshift tests were conducted with CNC suspensions deposited on UV-patterned ITO-coated glass (circular patterns with d = 6 mm). The tested concentrations were 0, 12.5, 25, and 50 mmol kg$_{CNC}^{-1}$, henceforth CNC0, CNC12.5, CNC25, and CNC50, respectively. **Figure 2**a–h shows the optical characterization results for these samples by POM. Reflectance spectra were taken during POM imaging (Figure 2a–f) through LCPL and RCPL filters (see Figure S3, Supporting Information). Calculating ΔCPL through Equation (1) and plotting them in Figure 2g a clear blueshift is observed for CNC0 through CNC25 from 620 to 510 nm, respectively, while maintaining
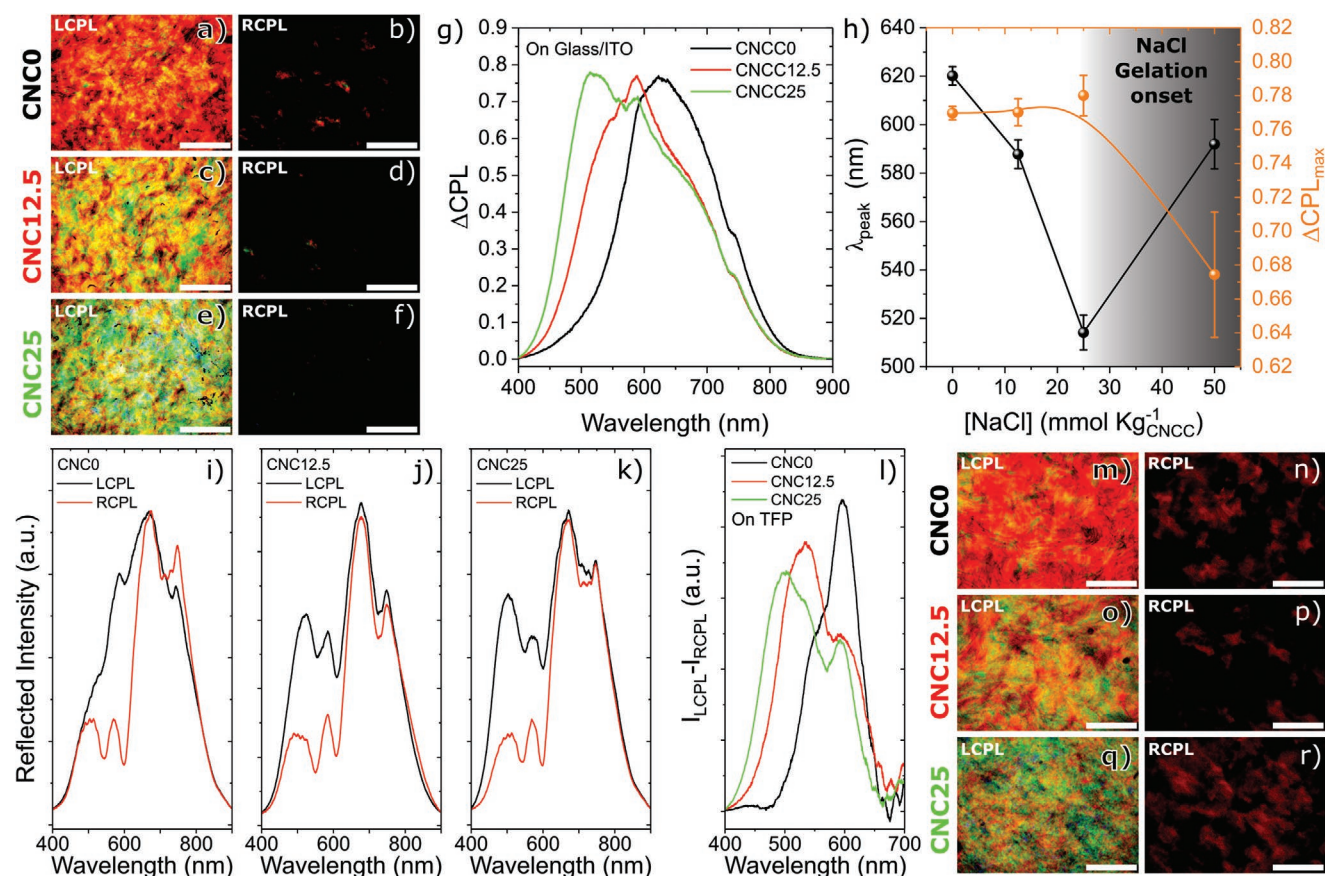

Figure 2. Optical characterization of CNC films on glass/ITO substrates and on TFPs with different NaCl concentrations. a–f) LCPL and RCPL POM images of CNC films on glass/ITO substrate with 0, 12.5, and 25 mmol kg$_{CNC}^{-1}$, respectively (scale bars indicate 200 μm), and g) their respective ΔCPL. h) Crucial optical parameters as a function of added NaCl, extracted from (g), such as λ_{peak} and ΔCPL$_{max}$ with indication of the onset of gelation for excess NaCl concentration. The lines are merely a visual guide. i–k) Individual reflectance spectra for TFP_CNC0, TFP_CNC12.5, and TFP_CNC25 structures and l) data compilation ($I_{LCPL} - I_{RCPL}$). m–r) POM images of the same samples through LCPL and RCPL.

Table 1. Summary of the used conditions to obtain films with three distinct photonic band gaps on glass/ITO and a comparison to the same suspensions on the TFP. Values represent averages taken from at least three samples.

Sample	NaCl [mmol kg$_{CNC}^{-1}$]	λ_{peak} on glass/ITO [nm]	λ_{peak} on TFP [nm]
CNC0	0	620	582
CNC12.5	12.5	588	549
CNC25	25	514	530

ΔCPL at around 80% (see also Figure 2h). As seen in Figure 2h, CNC50 samples showed a gelation behavior with a significant loss in ΔCPL and data in Figure 2g is, therefore, omitted for graph clarity (accessible in Figure S3, Supporting Information). From here on, complete device structures will be treated as TFP_CNCX, where X denotes the NaCl concentration.

Considering the same suspensions but self-assembled on the TFPs, a clear reflection from the underlying silicon is observed (mostly for 600 nm ≤ λ ≤ 900 nm, Figure 2i–k). These reflections are conspicuously accounted for by determining I_{LCPL}–I_{RCPL} to obtain λ_{peak} for each film (Figure 2l). **Table 1** compares the obtained data from Figure 2g,l and evidences a 9% decrease in λ_{peak}, indicating the capability for applications in a wider wavelength range.

Discrepancies between λ_{peak} on glass/ITO and on the TFPs are conjectured to arise from differences in surface area roughness between the two. Whereas glass/ITO presents a flat surface, the TFPs show micrometer-sized steps coming from its various layers. As these irregularities are on the same order of magnitude as the overall thickness of the CNC film the self-assembly process is influenced and may impact the projected λ_{peak}.[38]

2.1. Spectral Response: Experimental versus Simulation

As seen beforehand the employed CNC films act as a photonic filter for the two CP states. This in turn means that, when applied on top of a TFP, we can distinguish between LCPL and RCPL input signals by analyzing the I_{ph} of the devices. In the area of solar cells several approaches have been undertaken with photonic layers, such as films structured with wavelength-sized light-trapping features, positively influencing their efficiency.[39] Consequently, these types of devices are a perfect platform to give crucial insight into mesoporous photonic structures. By depositing CNC films on top of such devices it is possible to combine fundamental solar cell knowledge as a way of gaining insight into essential questions regarding self-assembly of CNCs, their orientation, domain formation or pitch distribution. These central questions are in focus by the scientific community working on CNCs as they can provide pertinent information in this still very young research field. Once knowing the output of a TFP with an integrated CNC film, one can take the results of a different device with a distinct CNC film to obtain its photonic parameters through reverse engineering and simulation. Consequently, solar cell simulation through finite-differences time domain (FDTD) methods might present an excellent approach to better understand chiral nematic CNC structures.

The FDTD method is a widely employed numerical approach to solve Maxwell's equations in order to evaluate the behavior of light in complex electromagnetic problems.[40–42] Moreover, this method benefits from its inherent capability of simulating nonlinear effects and material anisotropy,[43] thus making it an ideal choice to tackle complex materials, for instance liquid crystalline ones, in this case, the obtained chiral nematic CNC films. The simulations were aimed at comparing the theoretical and experimental behaviors. It should be noted that the FDTD results are purely optical, i.e., they do not account for carrier recombination and other electrical losses inside the solar cells. However, for this specific purpose, since a relative difference between two measurements is studied—RCPL and LCPL (according to Equation (1))—this is an accurate approximation as the main difference between the results is the magnitude of the optical signals.

Figure 3a shows the experimental SR for the TFP_CNC structure with distinct NaCl concentrations. In general, they show highest SR for 550 ≤ λ ≤ 600 nm, which also constitutes the region where the photonic band gap shift is induced through NaCl addition. Furthermore, and as expected, a striking difference in SR between LCPL and RCPL is observed. The filled curves depict the achieved ΔCPL, and thus indicate how much difference in I_{ph} could be achieved by changing from RCPL to LCPL for λ_{peak} with a specific power (around 50%).

To achieve simulation results that resemble most closely the experimental ones, a CNC film with a perfect pitch (λ_{peak} = 575 nm) was initially simulated, as shown in Figure 3b. The perfect pitch case clearly demonstrates the expected behavior of these materials, particularly the sharp peak at $\lambda \approx$ 575 nm, representing a drastic decrease in SR upon incidence of LCPL at this wavelength, as a consequence of its interaction with the CNC layer (see Video S1, Supporting Information). Similar results have been achieved by employing the Berreman method to simulate chiral nematic liquid crystals, showing the validity of the FDTD method used here.[44,45] Subsequently, in order to better approach the experimental results, a spatially varying pitch along the CNC layer was added (as depicted and explained in Figure S4, Supporting Information). The experimental measurements of ΔCPL shown in Figure 3a closely follow a Gaussian profile. Considering this, it was proposed that this behavior could be related with the fabricated CNCs' pitch dispersion. Keeping this in mind, the wavelength center (λ_{peak}) and standard deviation obtained from the fitting of these results were used as a foundation to implement the spatial pitch variation in the simulation, as thoroughly explained in Figure S5, Supporting Information. The adopted model (as schematized in Figure 3c) employs the TFP, a 7 µm parylene layer, a 100 nm SiO$_2$ thin film, and a 10 µm CNC layer.

Hence, in accordance with the experimentally measured results and their Gaussian fittings, the SR and reflectance for TFP_CNCX (with X = 0, 12.5, and 25) structures in RCPL and LCPL were simulated together with their respective ΔCPL, with the main results being shown in Figure 3d–f. Details on the simulation methodology, such as material properties, and further results are provided in Figure S6, Supporting Information.

Figure 3d compares the SR of the simulated and the experimental data for LCPL and RCPL of a TFP_CNC0 structure, where a striking resemblance between the two can be verified.
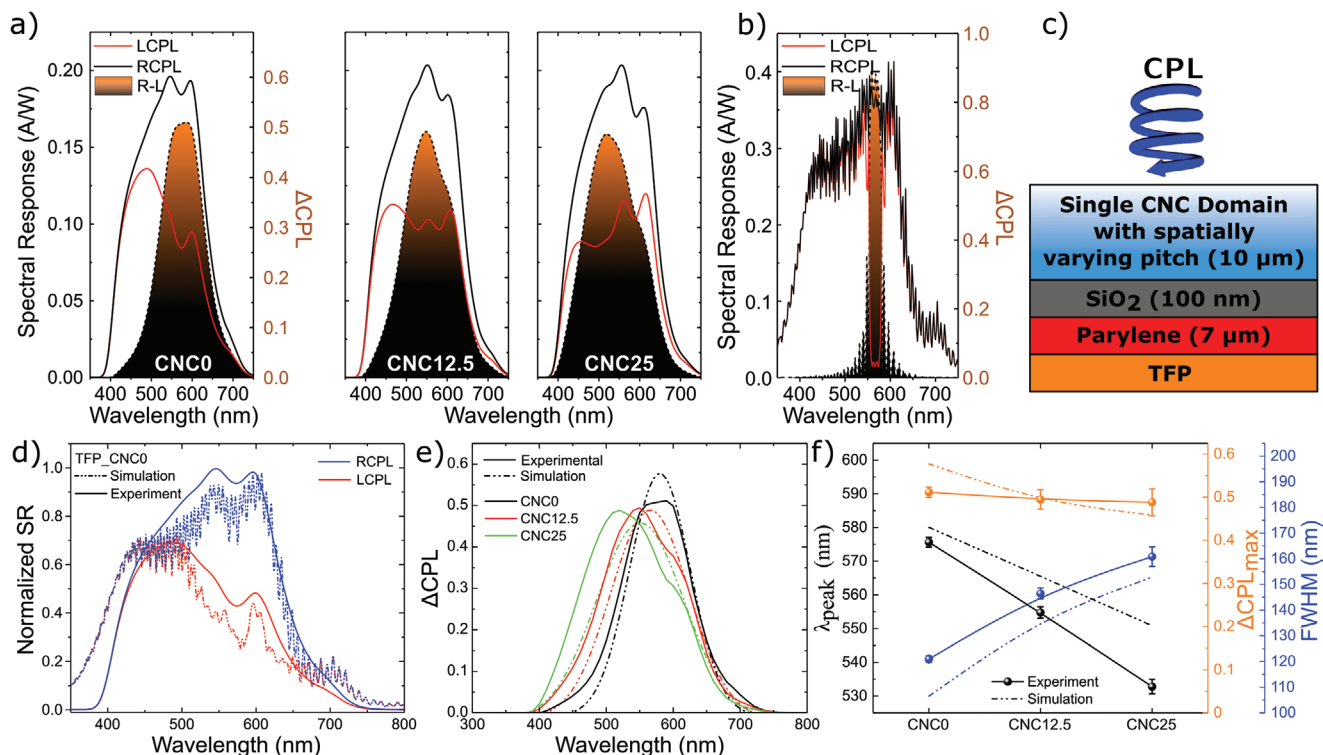
ADVANCED
SCIENCE NEWS
www.advancedsciencenews.com

ADVANCED
OPTICAL
MATERIALS
www.advopticalmat.de

Figure 3. SR of the devices and simulation. a) SR of TFP_CNCX (with X = 0, 12.5, and 25) structures for the three investigated NaCl concentrations for LCPL and RCPL (red and black curves, respectively). The filled curves show the calculated ΔCPL. b) Initial simulation results for a perfect pitch case. c) A schematic of the model used for the simulations. d) Comparison between the simulation and experimental results of a TFP_CNC0 structure. e) Comparison of the ΔCPL between the obtained experimental (continuous lines) and the simulated (dashed lines) results for the three NaCl concentrations. f) Comparison of the obtained parameters for the Gaussian fits of each curve in (e), such as the maximum photonic band gap (λ_{peak}), maximum CPL response (ΔCPL$_{max}$), and FWHM. Continuous and dashed lines are a visual guide and represent experimental and simulated results, respectively.

The experiment deviates slightly from the simulation results when entering the blue region ($\lambda < 450$ nm), which can be attributed to a decrease in transmittance by the used polymeric circular polarizers. Figure 3e shows a comparison of ΔCPL between simulated and experimental results for the three studied cases (CNC0, CNC12.5, and CNC25). Here, it should be noted that the simulation curves are merely fittings to the calculated ΔCPL from SR data of RCPL and LCPL of the FDTD results, with complete results being provided in Section S7, Supporting Information. Figure S7, Supporting Information, presents several sharp light interference peaks, due to the large thickness of the simulated layer relative to the wavelengths, which become smoothed in experimental characterization as a consequence of the inevitable nonuniformity of the physical properties of the measured materials.

The simulated results in Figure 3e show a theoretical behavior, with a decrease in pitch, akin to the experimental ones, especially a blueshift of the Gaussian peak. Furthermore, it is interesting to see a contrasting behavior between the left and right tails of the various profiles. While the right tail always remains stationary—similarly to the experimental results—the left tail gets blueshifted—also in accordance with the experimental results.

From Figure 3e, specific parameters can be extracted, such as ΔCPL$_{max}$, λ_{peak}, and the full width at half maximum (FWHM), giving insight into the spectral width of the CNCs'

photonic band gap. These parameters (experimental and simulated) are represented in Figure 3f, as a function of NaCl concentration. Concerning the experimental observations, the band gap blueshifts upon NaCl addition to the suspension. Nonetheless, the CPL response remains similar for all three presented concentrations, leading to the conclusion that we are facing no loss in self-assembly capabilities; the chiral nematic structure is successfully maintained (no gelation). FWHM increases as probably more monodomains with distinct pitches are formed by increasing the NaCl concentration, which, however, does not impair the overall performance of the devices.[46]

Similar trends are observed in the computational results, with minor discrepancies arising in a difference between theoretical and experimental results in the obtained blueshift (λ_{peak}). Several factors, such as the small ledge observed mostly on the right tail of the experimental profiles (see Figure 3e) for CNC12.5 and CNC25, that redshifted the Gaussian fittings and thence the average and standard deviation values that are at the basis of the simulations. Another factor might stem from the simplicity of the used model to evaluate the spatially varying pitch in a singular monodomain (Figure 3c), resulting in a difference between the real complex variation of a multidomain CNC's pitch and the one created by the employed simplified method (single domain method). Naturally, increasing the complexity of the model would help the accuracy of the results; however, the added computational cost to achieve these results
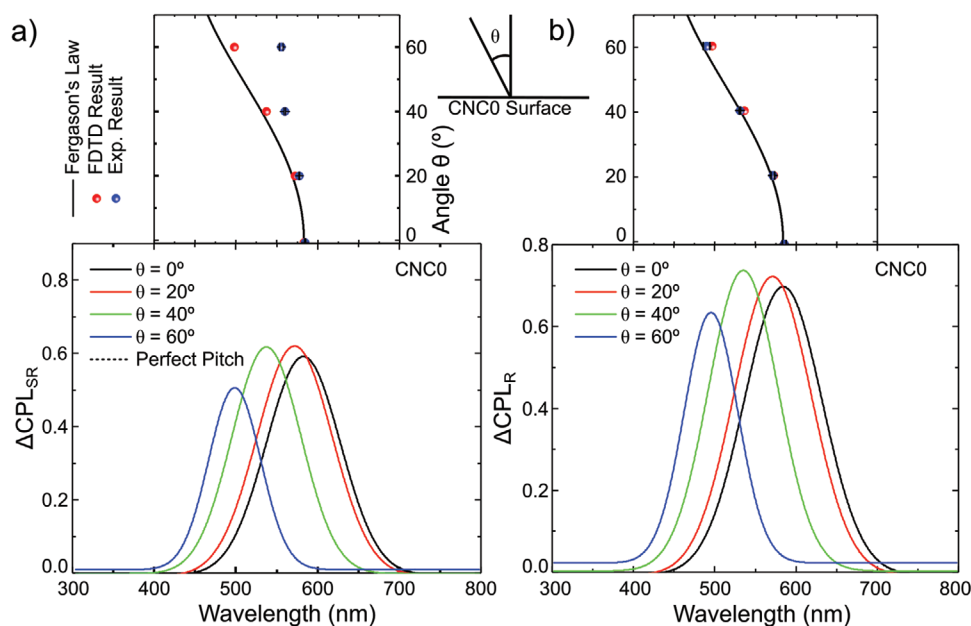
ADVANCED
SCIENCE NEWS
www.advancedsciencenews.com

ADVANCED
OPTICAL
MATERIALS
www.advopticalmat.de

Figure 4. Comparison of experimental, simulated, and theoretical results (Fergason's law) of angular response for a TFP_CNC0 structure. a) ΔCPL of SR for various angles of $\theta = (0°, 20°, 40°, 60°)$ (black, red, green, and blue). For a perfect CNC layer without pitch dispersion or defects at $\theta = 0°$ (dashed black curve). b) ΔCPL of reflectance for the same angles as in (a). Both graphical insets compare the progress of λ_{peak} with increasing angles (for simulated and experimental results) with values projected by Fergason's law (black curve).

would not bring any additional meaningful details to those already obtained.

2.2. Comparison to Fergason's Law

In order to further verify the obtained results by simulation, a TFP_CNC0 structure was analyzed on behalf of ΔCPL in SR and reflectance for different angles of light incidence. The obtained λ_{peak} values were then used for a comparison with experimental data and values predicted by Fergason's law defined as follows[47]

$$\lambda_{ref} = n_{av} p \cos\left(\beta + \sin^{-1} \frac{\sin \theta}{n_{av}} \right) \qquad (2)$$

here, λ_{ref} is the reflected wavelength, n_{av} is the average refractive index of the material, β is the angle between the orientation vector of the liquid crystal and the surface normal (0 for this case), p is the pitch of the chiral nematic structure, and θ is the light incidence angle—as shown schematically in the inset of **Figure 4**. Here, the similar behavior between the FDTD results and the Fergason's law is noticeable, further establishing the validity of this method for detailed studies of chiral nematic structures, such as CNCs. When compared to experimental results, it becomes evident that for the electrical characterization (angular SR—blue dots in Figure 4a) similarities to Fergason's Law are only met for small angles (0° and 20°), deviating from the predicted values, when increasing the angle of incidence. This can be explained by the pure optical prediction of Fergason for chiral nematic structures, as opposed to electrical results of the TFPs' SR outputs. These are influenced

by an assortment of electrical losses, resulting in deviations of photogenerated current from the optimal value at 0° incidence (which coincides with the law). However, considering pure optical effects (reflectance) of a TFP_CNC0 structure (see blue dots in Figure 4b—for full reflectance curves see Figure S8, Supporting Information), the results follow more accurately the predictions of Equation (2).

2.3. Applications for TFP_CNC Structures

As the TFP_CNC0 structures usually yield the highest CPL response, they are the devices of choice to study direct applications, involving CPL response. **Figure 5**a shows the transient response of a TFP_CNC0 structure for two distinct irradiation wavelengths ($\lambda_{red} = 617$ nm and $\lambda_{blue} = 470$ nm) and a cold white light source (with powers of 10.2, 17.2, and 21.5 mW, respectively). As expected, outside the photonic band gap of the CNC0 film (for λ_{blue}) only a marginal response is observed between the two different CPs (6.4%), whereas inside (for λ_{red}), this value rises to above 70%. The response is very fast, while reaching photogenerated currents on the order of tenth of microampere.

Another application for the devices developed in this work lies in the area of humidity sensing. There are several studies devoted to the investigation of pitch variations with humidity as CNC structures are hygroscopic and increase pitch upon exposure, resulting in a redshift of the photonic band gap.[48] While irradiating a TFP_CNC0 structure with LCPL inside the photonic band gap, a specific low state current is measured as most of the LCPL is reflected by the CNC0 layer. When humidity is increased the pitch increases up to 100 nm (see Figure S9, Supporting Information) and consequently
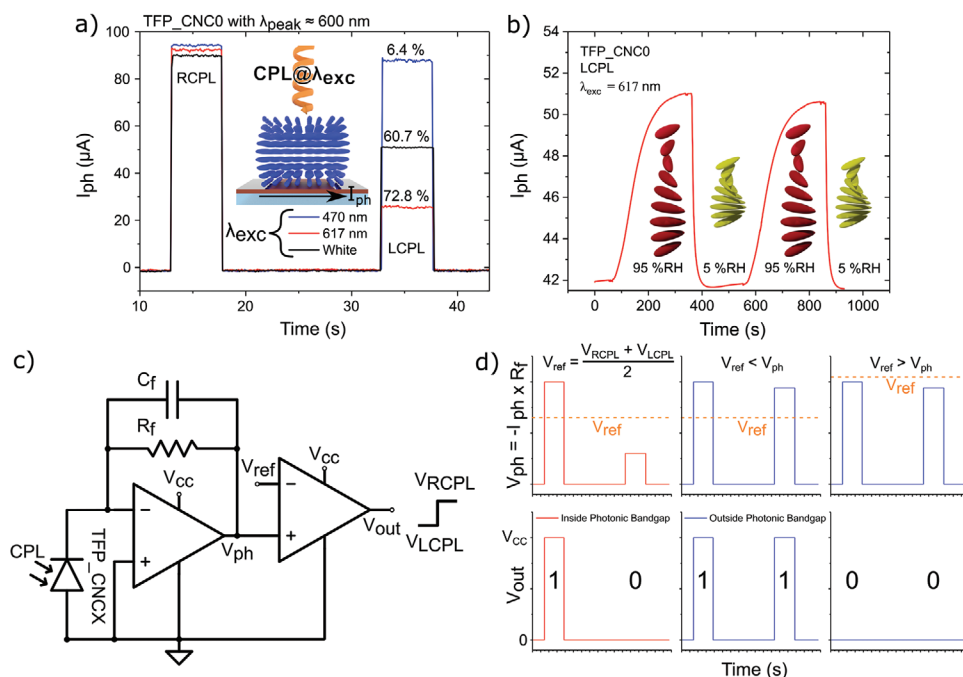
ADVANCED
SCIENCE NEWS
www.advancedsciencenews.com

ADVANCED
OPTICAL
MATERIALS
www.advopticalmat.de

Figure 5. Applications of a developed TFP_CNC0 structure. a) Transient response of I_{ph} for RCPL and LCPL at irradiation wavelengths of 617 and 470 nm and a white light source. A schematic illustrates the setup. b) Humidity response between 95 and 5 relative humidity (%RH) at LCPL (with $\lambda = 617$ nm). c) Circuit diagram of a transimpedance amplifier connected to a comparator in order to transform the TFP's CPL response into logic values. d) Example of logic value output for the circuit schematic in (c). Values are adapted from the transient response in (a).

the maximum ΔCPL (filled curves in Figure 3a) is shifted into the infrared region. It follows that for the initial $\lambda_{exc} = 617$ nm more light is transmitted and I_{ph} increases to a high state. The process is reversible as evidenced by two cycles between 95% and 5% RH, showing an optical memory effect. The schematics of Figure 5b depict the expansion and relaxation of the CNC structure between the two states. The response is quite slow; it can, however, be drastically increased by decreasing the thickness of the deposited CNC layer.[44]

The signal processing between LCPL and RCPL could be achieved with a transimpedance operational amplifier (OpAmp) coupled to a comparator, as depicted in Figure 5c, capable of amplifying and converting a current input into a digital voltage output. This amplifier has a low frequency gain of $-R_f$, the feedback resistance of the OpAmp. In this configuration, the capacitor C_f serves merely to stabilize the gain at those lower frequencies. Consequently, the OpAmp feeds distinct V_{ph} values to the comparator, depending on the polarization state of the incident light. As V_{ph} during RCPL and LCPL irradiation will be over 50% distinct (see Figure 5a) and with V_{ref} properly defined (ideally in between the two values, Figure 5d), it is possible to have distinct logic outputs for the two states as follows:

- If LCPL → V_{out} = Low = 0 V
- If RCPL → V_{out} = High = V_{CC}

Naturally, these two conditions depend on whether the irradiation wavelength lies inside the photonic band gap of the CNC film or not. Outside the band gap, these values are independent from the CP states and will either give a HIGH or a LOW value, depending on the defined V_{ref} (see Figure 5d). This

type of signal processing is crucial for the application of such devices in sensing, imaging, optoelectronic anti-counterfeiting but also information technology, where distinct circular polarization states can give specific logic values.

3. Conclusions

The present work shows the possibility to combine photonic CNC structures with TFPs to obtain devices capable of detecting and converting CPL into distinct photogenerated currents (I_{ph}). Due to a self-assembly process, the CNC films develop into a left-handed chiral nematic structure with ordering on the nanoscale, resulting in left-handed circular Bragg reflection of light (CPL) in the visible spectrum. Such structures consequently reflect LCPL and transmit RCPL. The integration of these photonic structures into TFPs enables transducing the CPL response for practical applications. The pristine CNC films show a photonic band gap of around 600 nm, in order to extend possible applications, specific amounts of NaCl are added into the CNC suspension to induce band gap blueshifts in the final films. The devices are characterized on behalf of their SR, giving a maximum $SR_{RCPL} = 184.8$ mA W^{-1} and $SR_{LCPL} = 84.6$ mA W^{-1}, resulting in photogenerated currents that are over 50% distinct between LCPL and RCPL for the same incident light power. The FDTD method was used to simulate the photonic structures. Simulation results follow closely the experimental ones, where a photonic band gap blueshift upon NaCl addition is also observed. Further confirmation of the modeled results is gained through angular SR and reflectance, where the simulations follow Fergason's Law on the reflected wavelength

variation for distinct angles of chiral nematic liquid crystals. Experimental results show agreement for angular reflectance but not for SR, as the latter is based on electrical results as opposed to the optical law established by Fergason. The developed CPL sensors show applicability in fast CPL response inside their photonic band gap, where over 50% distinct currents (on the order of tenth of microampere) are generated for RCPL and LCPL. Due to the hygroscopic character of the CNC structure, humidity induces swelling and increases the chiral nematic pitch, resulting in a shift of the photonic band gap. Cycling between low and high humidity states, the devices show distinct photogenerated currents, when continuously irradiated with LCPL inside their photonic band gap, due to a dislocation of the maximum SR_{LCPL}. The reported devices thus show potential for their use in imaging with polarized light, CPL sensing, optoelectronic counterfeiting, and information processing with added degrees of freedom through the gain of additional logic states connected solely to the handedness of the CPL.

4. Experimental Section

Device Fabrication: The TFPs were optimized and fabricated as reported elsewhere.[49] The TFP was subsequently passivated with a 7 µm thick Parylene-C (deposited through chemical vapor deposition using a Specialty Coating System Model PDS 2010 Labcoter 2) layer to protect the aluminum contacts from oxidization that could occur by the CNC suspension. This was followed by electron beam deposition of a circular ($d = 6$ mm) 100 nm SiO_2 thin film exactly above the active area of the device to create a hydrophilic region on the hydrophobic Parylene-C. With this, a well was created, where the CNC suspension only spreads until the limit of the SiO_2 film, staying contained within the 6 mm circle (see Figure 1d). The CNCs were received from CelluForce as sodium neutralized spray-dried powder (2017 NCV-100). To prepare a 100 g stock batch suspension of 5 wt%, first, 5 g of as-received CNC powder was slowly added to 95 g of H_2O in a beaker, under vigorous magnetic stirring, which continued for 2 h at 1200 rpm. After this, 15 g of stock batch was transferred to a flat-bottomed glass vial and subjected to tip sonication until 5.4 kJ g_{CNC}^{-1} of energy input was reached. The used sonication system was a 500 W Sonics Vibra-Cell (VC-505) by Thermo Fisher Scientific with a 6 mm wide tapered sonication tip at 60% power with 1 s on and 1 s off pulses. After sonication, the suspension was transferred to a glass test tube and left standing upright for at least 1 week to induce phase separation. After phase separation into a lower anisotropic and an upper isotropic phase (anisotropic volume fraction of 50%), the two phases were physically separated from each other with a Pasteur pipette. The anisotropic suspension was filtered through a 10 µm pore fiber glass filter after which it was sealed, stored in the fridge at 4 °C, and ready to use. The CNCs were 181 ± 62 nm long and 4 ± 1 nm wide (determined through AFM measurements) with a sulfur content of 35% ± 2% atomic concentration (determined through elemental analysis). To prepare the NaCl samples, a 1 M NaCl solution was prepared and the necessary volume was added to 1 g of 5 wt% CNC suspension into an Eppendorf that underwent vigorous vortexing for 5 min to ensure mixing. After drop-casting 10 µL of CNCX suspension (where X = 0, 12.5, or 25 mmol kg_{CNC}^{-1}), the devices are stored in a high-humidity (relative humidity > 95%) and low-temperature ($T = 4$ °C) environment to induce self-assembly. The drying process takes about 48 h, after which the active photodiode area was covered by a photonic iridescent film with around 10 µm of thickness (see Figure 1e,f for a schematic representation and photograph, respectively). The samples were stored in a controlled environment ($T = 21$ °C, relative humidity = 25%) until further characterization.

Polarized Optical Microscopy: POM images were obtained in reflection mode, by using an Olympus BX51 microscope, coupled with an Olympus DP73 CCD camera, and acquired with the Stream Basic v.1.9 Olympus software. A cold illumination source generated by a halogen lamp (KL 2500 LCD, Olympus) was used. The images were obtained with ×10 objectives (Olympus, MPlanFL N). To detect the reflection of right-handed and left-handed circularly polarized light, a quarter waveplate (U-TP137, Olympus) coupled with a polarizer was inserted in the optical path. To obtain reflectance spectra of the observed area, a standard UV–vis–NIR spectrometer (200 nm $\leq \lambda \leq$ 1050 nm) coupled to a halogen tungsten light source was connected to the microscope and combined with LightScan software by Sarspec. Spectra were taken in LCPL and RCPL in absolute reflected intensity.

Spectral Response (and Angular) Measurements: The SR measurements were performed using a Newport QuantX-300 system, equipped with a xenon lamp of 100 W, with a nominal illumination spot size of 0.8 × 1.1 mm. The used software for measurements was QuantX. The devices were mounted on a rotary stage for angular measurements. Circular polarizers by Edmund Optics (left or right) were introduced in the light beam path to induce the desired polarization.

Angular Reflectance Spectrophotometry: Angular reflectance was measured by a PerkinElmer Lambda 950 UV–vis–NIR high-performance double-beam dual monochromator spectrometer. Wavelength range was adjusted between 400 and 800 nm. For this range, a photomultiplier type R 6872 was used as the detector. An integrating sphere was used with an adjustable angular mount reaching from 0° to 360 °. Circular polarizers by Edmund Optics (left or right) were introduced in the light beam path to induce the desired polarization.

Transient CPL and Humidity Sensing: CPL characterization and humidity sensing was performed using the same standard UV–vis–NIR spectrometer (200 nm $\leq \lambda \leq$ 1050 nm) by Sarspec for reflectance characterization during POM, but for this case, coupled to fiber-coupled LEDs (617 nm, 470 nm, and cold white light) from Thorlabs with 10.2, 17.2, and 21.5 mW of power, respectively. Circular polarizers by Edmund Optics were positioned in the light beam to obtain the desired polarization. The photogenerated current was measured in transient mode using an Agilent 4155C semiconductor parameter analyzer connected to a NEXTRON Micro Probe Station with a fused silica viewport. For humidity sensing, nitrogen flux through a bubbler system connected to a flowmeter was used to control the relative humidity inside the NEXTRON 100 cm^3 chamber. Humidity was measured inside the chamber externally with a DHT11 Arduino-coupled humidity sensor.

Supporting Information

Supporting Information is available from the Wiley Online Library or from the author.

Conflict of Interest

The authors declare no conflict of interest.

[1] A. Ozcelik, R. Pereira-Cameselle, N. P. Ulrih, A. G. Petrovic, J. L. Alonso-Gómez, *Sensors* **2020**, *20*, 974.

[2] T. D. Stephens, C. J. W. Bunde, B. J. Fillmore, *Biochem. Pharmacol.* **2000**, *59*, 1489.

[3] M. Kadic, G. W. Milton, M. van Hecke, M. Wegener, *Nat. Rev. Phys.* **2019**, *1*, 198.

[4] M. I. Stockman, K. Kneipp, S. I. Bozhevolnyi, S. Saha, A. Dutta, J. Ndukaife, N. Kinsey, H. Reddy, U. Guler, V. M. Shalaev, A. Boltasseva, B. Gholipour, H. N. S. Krishnamoorthy, K. F. MacDonald, C. Soci, N. I. Zheludev, V. Savinov, R. Singh, P. Groß, C. Lienau, M. Vadai, M. L. Solomon, D. R. Barton, M. Lawrence, J. A. Dionne, S. V. Boriskina, R. Esteban, J. Aizpurua, X. Zhang, S. Yang, D. Wang, W. Wang, T. W. Odom, N. Accanto, P. M. de Roque, I. M. Hancu, L. Piatkowski, N. F. van Hulst, M. F. Kling, *J. Opt.* **2018**, *20*, 043001.

[5] W. Li, Z. J. Coppens, L. V. Besteiro, W. Wang, A. O. Govorov, J. Valentine, *Nat. Commun.* **2015**, *6*, 8379.

[6] T. Gehrke, *J. Nanophotonics* **2008**, *2*, 021990.

[7] T. H. Chiou, S. Kleinlogel, T. Cronin, R. Caldwell, B. Loeffler, A. Siddiqi, A. Goldizen, J. Marshall, *Curr. Biol.* **2008**, *18*, 429.

[8] T. Labhart, *J. Exp. Biol.* **1996**, *199*, 1467.

[9] S. Rossel, R. Wehner, *Nature* **1986**, *323*, 128.

[10] G. Horváth, *Polarized Light and Polarization Vision in Animal Sciences*, Springer-Verlag Berlin Heidelberg, Berlin **2014**, pp. 217–224.

[11] Y. K. Takahashi, R. Medapalli, S. Kasai, J. Wang, K. Ishioka, S. H. Wee, O. Hellwig, K. Hono, E. E. Fullerton, *Phys. Rev. Appl.* **2016**, *6*, 054004.

[12] M. Grell, M. Oda, K. S. Whitehead, A. Asimakis, D. Neher, D. D. C. Bradley, *Adv. Mater.* **2001**, *13*, 577.

[13] J. Gilot, R. Abbel, G. Lakhwani, E. W. Meijer, A. P. H. J. Schenning, S. C. J. Meskers, *Adv. Mater.* **2010**, *22*, E131.

[14] E. Ogut, G. Kiziltas, K. Sendur, in *2009 IEEE LEOS Annual Meeting Conference Proceedings*, IEEE, Turkey **2009**, pp. 160–161.

[15] S. Richtberg, R. Girwidz, *Phys. Teach.* **2017**, *55*, 406.

[16] K. Miyamoto, H. Wortelen, T. Okuda, J. Henk, M. Donath, *Sci. Rep.* **2018**, *8*, 10440.

[17] J. F. Revol, H. Bradford, J. Giasson, R. H. Marchessault, D. G. Gray, *Int. J. Biol. Macromol.* **1992**, *14*, 170.

[18] J. F. Revol, L. Godbout, D. G. Gray, *J. Pulp Pap. Sci.* **1998**, *24*, 146.

[19] O. J. Rojas, *Cellulose Chemistry and Properties: Fibers, Nanocelluloses and Advanced Materials*, Springer International Publishing, Cham, Switzerland **2016**, pp. 287–328.

[20] C. Schütz, J. R. Bruckner, C. Honorato-Rios, Z. Tosheva, M. Anyfantakis, J. P. F. Lagerwall, *Crystals* **2020**, *10*, 199.

[21] X. Mu, D. G. Gray, *Cellulose* **2015**, *22*, 1103.

[22] M. Arcari, E. Zuccarella, R. Axelrod, J. Adamcik, A. Sánchez-Ferrer, R. Mezzenga, G. Nyström, *Biomacromolecules* **2019**, *20*, 1288.

[23] S. J. Hanley, J.-F. Revol, L. Godbout, D. G. Gray, *Cellulose* **1997**, *4*, 209.

[24] P. Grey, S. N. Fernandes, D. Gaspar, E. Fortunato, R. Martins, M. H. Godinho, L. Pereira, *Adv. Funct. Mater.* **2018**, *29*, 1805279.

[25] M. Giese, M. Spengler, *Mol. Syst. Des. Eng.* **2019**, *4*, 29.

[26] A. T. Vicente, P. J. Wojcik, M. J. Mendes, H. Águas, E. Fortunato, R. Martins, *Sol. Energy* **2017**, *144*, 232.

[27] M. Alexandre, M. Chapa, S. Haque, M. J. Mendes, H. Águas, E. Fortunato, R. Martins, *ACS Appl. Energy Mater.* **2019**, *2*, 2930.

[28] Lumerical, Inc., https://www.lumerical.com/ (accessed: May 2020).

[29] P. X. Wang, W. Y. Hamad, M. J. MacLachlan, *Nat. Commun.* **2016**, *7*, 11515.

[30] M. A. Green, M. J. Keevers, *Prog. Photovoltaics* **1995**, *3*, 189.

[31] R. M. Parker, G. Guidetti, C. A. Williams, T. Zhao, A. Narkevicius, S. Vignolini, B. Frka-Petesic, *Adv. Mater.* **2018**, *30*, 1704477.

[32] C. D. Edgar, D. G. Gray, *Cellulose* **2001**, *8*, 5.

[33] X. M. Dong, T. Kimura, J.-F. Revol, D. G. Gray, *Langmuir* **1996**, *12*, 2076.

[34] C. Honorato-rios, C. Lehr, C. Schütz, R. Sanctuary, M. A. Osipov, J. Baller, J. Lagerwall, *NPG Asia Mater* **2018**, *10*, 455.

[35] A. Gençer, J. Van Rie, S. Lombardo, K. Kang, W. Thielemans, *Biomacromolecules* **2018**, *19*, 3233.

[36] Y. Liu, C. Schütz, G. Salazar-Alvarez, L. Bergström, *Langmuir* **2019**, *35*, 3600.

[37] D. G. Gray, *Philos. Trans. R. Soc., A* **2018**, *376*, 20170038.

[38] B. L. Tardy, B. D. Mattos, L. G. Greca, T. Kämäräinen, K. W. Klockars, O. J. Rojas, *Adv. Funct. Mater.* **2019**, *29*, 1808518.

[39] O. Sanchez-Sobrado, M. J. Mendes, S. Haque, T. Mateus, H. Aguas, E. Fortunato, R. Martins, *J. Mater. Chem. C* **2019**, *7*, 6456.

[40] M. J. Mendes, A. Araújo, A. Vicente, H. Águas, I. Ferreira, E. Fortunato, R. Martins, *Nano Energy* **2016**, *26*, 286.

[41] S. Haque, M. J. Mendes, O. Sanchez-Sobrado, H. Águas, E. Fortunato, R. Martins, *Nano Energy* **2019**, *59*, 91.

[42] M. Chapa, M. F. Alexandre, M. J. Mendes, H. Águas, E. Fortunato, R. Martins, *ACS Appl. Energy Mater.* **2019**, *2*, 3979.

[43] S. D. Gedney, *Introduction to the Finite-Difference Time-Domain (FDTD) Method for Electromagnetics*, Morgan & Claypool Publishers, San Rafael, CA **2011**.

[44] T. H. Zhao, R. M. Parker, C. A. Williams, K. T. P. Lim, B. Frka-Petesic, S. Vignolini, *Adv. Funct. Mater.* **2018**, *29*, 1804531.

[45] S. N. Fernandes, P. L. Almeida, N. Monge, L. E. Aguirre, D. Reis, C. L. P. de Oliveira, A. M. F. Neto, P. Pieranski, M. H. Godinho, *Adv. Mater.* **2014**, *29*, 094008.

[46] A. Hirai, O. Inui, F. Horii, M. Tsuji, *Langmuir* **2009**, *25*, 497.

[47] J. L. Fergason, *Mol. Cryst.* **1966**, *1*, 293.

[48] Q. Zhu, S. Liu, J. Sun, J. Liu, C. J. Kirubaharan, H. Chen, W. Xu, Q. Wang, *Carbohydr. Polym.* **2020**, *235*, 115933.

[49] O. Sanchez-Sobrado, M. J. Mendes, T. Mateus, J. Costa, D. Nunes, H. Aguas, E. Fortunato, R. Martins, *Sol. Energy* **2020**, *196*, 92.